ROYAL SOCIETY
OF CHEMISTRY

Check for updates

A robust conductive covalent organic framework for ultra-stable potassium storage†

Yu-Yang Li,‡[a] Ji-Miao Xiao,‡[b] Mo Xie, [ID][b] Lei-Feng Wu,[a] Yan-Fei Chen,[b] Shuai Yuan, [ID] *[a] De-Shan Bin*[b] and Jing-lin Zuo [ID] *[a]

Redox-active covalent organic frameworks (COFs) have garnered significant attention in the field of K-ion batteries (KIBs), but their applications are mainly hampered by their low electronic conductivity and insufficient cyclability owing to the large size of K-ions. Herein, we report a Ni-bis(dithiolene) and tetrathiafulvalene-based COF (Ni-TTF) with promising electronic conductivity and exceptional stability for high-performance KIB anodes. The redox-active units of Ni-bis(dithiolene) and tetrathiafulvalene (TTF) provide accessible sites for K-ion storage. The one-dimensional tunnel structure and good conductivity of Ni-TTF enabled fast charge (K^+/e^-) transfer. The reticular network structure maintained its stability in organic electrolyte and ensured a resilient electrode to sustain repeated K-ion intercalation/deintercalation. As a result, Ni-TTF delivered a high reversible capacity of 223 mA h g^{-1} over more than 800 cycles at a current density of 1C (0.3 A g^{-1}). Moreover, Ni-TTF achieved ultrastable cyclability, without discernible capacity fading after 2500 cycles at 2C, ranking it among the best organic anode materials for KIBs. This contribution opened a new avenue in the design of robust COFs with promising redox activity and improved conductivity for ultrastable K-ion storage.

Introduction

The continual advancement of rechargeable battery technologies is imperative to meet the escalating demand for portable electronics,[1] electric vehicles,[2] and grid-scale energy storage systems.[3] While lithium-ion batteries (LIBs) are currently the leading energy storage devices in the market, their sustainable growth faces challenges due to the limited (0.0017 wt% in the Earth's crust) and uneven distribution of lithium resources.[4] In this quest for alternatives, potassium-ion batteries (KIBs) have inspired considerable research interest as promising contenders owing to the abundant potassium resources (1.5 wt% in the Earth's crust) and their lower redox of the K^+/K redox couple (-2.93 V vs. the standard hydrogen electrode) close to -3.04 V (vs. SHE) of Li^+/Li.[5,6] However, the evolution of KIBs has been impeded by obstacles, particularly the inferior cycle stability,[7] primarily attributed to the larger ionic diameter of a K-ion (2.76 Å, in contrast to 1.52 Å of a Li-ion), leading to serious electrode volumetric expansion and rapid capacity fading during repeated K-ion intercalation. To surmount these challenges, extensive research has been dedicated to discovering suitable anode materials, including intercalation compounds,[8,9] graphitic carbon,[10,11] amorphous carbon,[12] MXenes,[13,14] and alloys.[5,15] However, these anodes have exhibited limitations in terms of cyclability. The pursuit of stable KIB anodes capable of sustaining thousands of K-ion intercalation and deintercalation cycles remains a formidable challenge.

Due to their abundant resources, flexible structure designability, and high level of functionality, organic anode materials have found great potential in the storage of a wide variety of metal cations (e.g., Li^+, Na^+, K^+, Mg^{2+}, and Al^{3+}). Typically, organic compounds or small molecules with diverse redox-active functional groups, such as C=O,[16] C=N,[17] C≡N,[18] and N=N,[19] have been explored as potential anode materials with high reversible capacity. Nonetheless, their inherent solubility in organic electrolytes, low conductivity, and limited pores hinder their cyclability and electrode kinetics. Accordingly, organic anodes for KIBs with favored characteristics, including robust chemical and mechanical stability, high insolubility, and promising conductivity, are highly desired. In this regard, covalent organic frameworks (COFs) have garnered substantial attention for their viability as rechargeable battery materials. In contrast to conventional organic compounds and small organic molecules, porous crystalline COFs, which are assembled through strong covalent bonds, possess inherent one-dimensional channels and demonstrate exceptional stability across various solvents,[20] thereby enhancing electrode kinetics

[a] State Key Laboratory of Coordination Chemistry, School of Chemistry and Chemical Engineering, Nanjing University, Nanjing, Jiangsu 210023, P. R. China. E-mail: syuan@nju.edu.cn; zuojl@nju.edu.cn

[b] College of Chemistry and Materials Science, Guangdong Provincial Key Laboratory of Functional Supramolecular Coordination Materials and Applications, Jinan University, Guangzhou 510632, P. R. China. E-mail: bindeshan@jnu.edu.cn

‡ Y.-Y. Li and J.-M. Xiao contributed equally.

This journal is © The Royal Society of Chemistry 2023

J. Mater. Chem. A, 2023, 11, 24661–24666 | 24661

and stability for K-ion storage.[21] Furthermore, the infusion of redox-active sites into COFs holds promise for high reversible capacity.[22] Despite these merits as battery anode candidates, the low electronic conductivity of COFs remains a major limiting factor for efficient electron transport, impeding the fast interaction between K ions and redox-active sites inside the skeleton. To address this issue, a common strategy involves compositing COFs with conductive materials such as carbon nanotubes[23] and graphene.[24] However, the preparation of COF/carbon composites usually requires strict and tedious operations, thus leading to a low fabrication efficiency. Meanwhile, while these endeavors have successfully augmented the conductivity of COF-based anode materials, they have also compromised the overall energy density of practical batteries due to the addition of carbon components. Consequently, the design of COFs as KIB anode materials should have an overall consideration of their high redox activity, fast K^+/e^- transfer, and excellent chemical/structural stability.

In this study, we present, for the first time, the use of a conductive redox-active COF (Ni-TTF) featuring Ni-bis(dithiolene) and tetrathiafulvalene (TTF) units for high-performance KIB anodes. Tetrathiafulvalene (TTF) and its derivatives have garnered substantial attention in organic electronics,[25] organic conductors,[26] and catalysis[27] due to their electron-rich nature and multiple reversible, stable redox states (TTF, $TTF^{\bullet+}$, and TTF^{2+}). For example, Dinca et al. reported several TTF-based MOFs that showed a face-to-face stack of TTF units, resulting in S···S interactions and an enhanced conductivity of 2.84×10^{-4} S cm^{-1}.[26] Liu et al. presented a TTF-based COF displaying a tunable electrical conductivity of 1.2×10^{-6} S cm^{-1} and 2.8×10^{-3} S cm^{-1} before and after I_2 oxidation, respectively.[28] On a parallel note, Ni-bis(dithiolene), an inorganic analog of TTF with Ni replacing the C=C segment, has exhibited redox activity with three readily accessible and stable oxidation states. Building upon this foundation, we expected that the incorporation of TTF and Ni-bis(dithiolene) into the COF skeleton would concurrently confer redox-active centers and electroconductivity, unlocking significant potential for KIB anode applications. As a KIB anode, these COFs can deliver a promising initial reversible capacity of 249 mA h g^{-1} at 0.2C and ultrastable cyclability. Remarkably, upon activation, this COF anode could promise a high reversible capacity of 223 mA h g^{-1} and sustain more than 800 cycles at 1C. Even on extending the cycling to 2500 cycles at a larger current density of 2C, this COF anode could deliver a reversible capacity of 150 mA h g^{-1} without capacity fading. This extraordinary cycling performance is one of the best performances among those for state-of-the-art organic KIB anodes. Aided by electrochemical probing and theoretical simulation, it was identified that the K-storage mechanism for this COF anode was governed by 10-electron redox activity for a covalent organic framework unit. Meanwhile, the existence of capacitive charge storage behavior for this COF can also be identified, which may benefit from the considerable specific surface area and continuous pores. This contribution provides insights into designing redox-active and highly robust COF materials for ultra-stable KIB anodes based on a reticular chemistry strategy.

Results and discussion

Ni-TTF was synthesized via an imine condensation reaction between Ni-bis(dithiolene)tetrabenzaldehyde [Ni(bded)$_2$] and tetra(aminophenyl)-tetrathiafulvalene (TTFNH$_2$) in o-dichlorohenzene and n-butanol (Fig. 1a).[29] The powder X-ray diffraction (PXRD) pattern of Ni-TTF exhibited a prominent peak at 5.3°, accompanied by minor peaks at 7.5°, 10.6°, 11.9°, 16.9°, and 26.0°. These peaks correspond to the crystallographic facets [110], [200], [220], [310], [240], and [001], respectively. Structural simulations revealed that Ni-TTF adopted a **sql** topology with an AA stacking arrangement (Fig. 1b). The crystal structure was characterized in the P222 space group with cell parameters $\alpha = \beta = \gamma = 90°$, $a = 23.57$ Å, $b = 23.43$ Å, and $c = 3.43$ Å. This simulated lattice excellently matched the experimental PXRD pattern, as evidenced by Pawley refinement, yielding $R_{wp} = 2.28\%$ and $R_p = 1.68\%$ (Fig. 1c).

Fourier transform infrared spectroscopy (FTIR) analyses illustrated significant changes in vibrational bands (Fig. S2†). Specifically, the disappearance of the N–H stretching band in the range of 3100–3500 cm^{-1} was attributed to TTFNH$_2$, alongside the pronounced weakening of the C=O peak at 1687 cm^{-1} linked to Ni(bded)$_2$, and the emergence of the C=N stretching peak at 1618 cm^{-1} in Ni-TTF collectively affirmed the successful formation of imine bonds. The surface morphology of Ni-TTF was examined using scanning electron microscopy (SEM), which unveiled irregular nano-/microparticles (Fig. 1d and S4†). High-resolution transmission electron microscopy (HRTEM) revealed that the rough surface of the particles could be attributed to the aggregation of nanoplates with diameters ranging from 100 to 200 nm (Fig. S5†). The energy dispersive spectroscopy (EDS) spectra proved the even distribution of C, N, S, and Ni in Ni-TTF (Fig. S6†). To assess the porosity of Ni-TTF, N$_2$ adsorption/desorption experiments were conducted at 77.3 K. These analyses revealed that Ni-TTF displayed a characteristic type I isotherm. The specific surface area, determined via the Brunauer–Emmett–Teller (BET) method, amounted to 521 cm^2 g^{-1} (Fig. 1e). Additionally, a pore width of 9.3 Å was estimated through pore size distribution calculations based on the density functional theory (DFT) model, correlating well with the 1D channel width inherent to the simulated AA stack of Ni-TTF (Fig. S3†). Thermal gravimetric analysis (TGA) of Ni-TFF in an air atmosphere within the temperature range between 50 and 600 °C at a heating rate of 10 °C min^{-1}, and no obvious mass loss was observed before the temperature reached 310 °C (Fig. S7†), demonstrating the high thermal stability of Ni-TTF. PXRD patterns of Ni-TTF were further tested following exposure to a diverse array of conditions to analyze its chemical stability, including soaking in various organic solvents and aqueous solutions with pH levels spanning from 1 to 14, and immersion in 5 M KSFI electrolyte in a 1 : 1 (volume ratio) mixture of ethylene carbonate (EC) and ethyl methyl carbonate (EMC) for 24 hours. Additionally, Ni-TTF underwent a heat treatment involving annealing at 300 °C for 5 hours under an Ar atmosphere, and no discernible alterations in the PXRD patterns were observed, confirming the exceptional thermal and
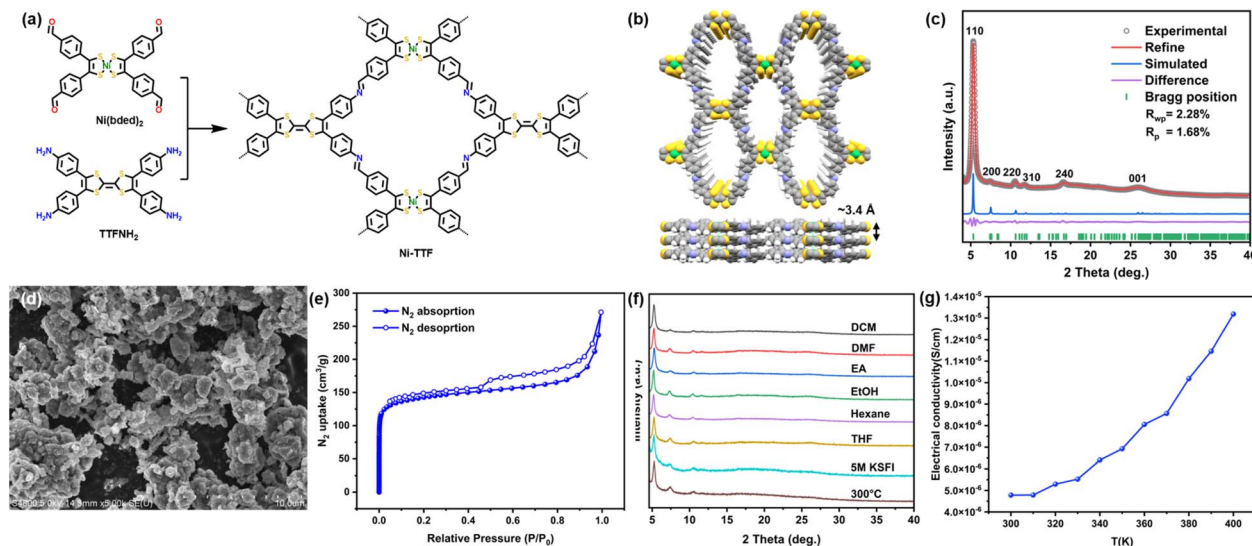
24662 | J. Mater. Chem. A, 2023, 11, 24661–24666

This journal is © The Royal Society of Chemistry 2023

Fig. 1 (a) Synthesis of Ni–TTF. (b) Top and side views of the simulated structure of Ni–TTF. (c) Pawley refinement and the PXRD pattern of Ni–TTF. (d) HRTEM image of Ni–TTF. (e) N$_2$ adsorption/desorption isotherm of Ni–TTF. (f) PXRD patterns showing stability of Ni–TTF. (g) Temperature dependent conductivity of Ni–TTF from 300 K to 400 K.

chemical stability of Ni-TTF (Fig. 1f). The temperature-dependent conductivity of Ni-TTF after annealing under the abovementioned conditions was determined, which showed the semiconductive behavior of Ni-TTF, with an electroconductivity increase from 4.78×10^{-6} to 1.32×10^{-5} S cm^{-1} within a temperature range from 300 to 400 K (Fig. 1g). The Tauc plot extracted from the UV-vis spectrum further proved the semiconductive nature of Ni-TTF with a narrow bandgap of 0.98 eV (Fig. S8†).

We then demonstrated the significant implications of the resultant Ni-TTF for high-performance KIB anodes. Notably, we

directly used the as-prepared bulk COF nano/microparticles as the active materials rather than the reported exfoliated few-layer COF product or carbon/COF composition. Fig. 2a shows the charge and discharge profiles obtained within a voltage range from 0 V to 3 V (vs. K$^+$/K). Ni-TTF exhibited a promising reversible specific capacity of 249, 232, and 227 mA h g^{-1} in the initial three cycles at 0.2C (1C = 300 mA g^{-1}). In rate performance tests, Ni-TTF exhibits promising reversible specific capacities of 273, 229, 178, 140, and 107 mA h g^{-1} at current densities of 0.1, 0.2, 0.5, 1, and 2C, respectively (Fig. 2b and S9†). When the current density returns to 0.2C, the reversible
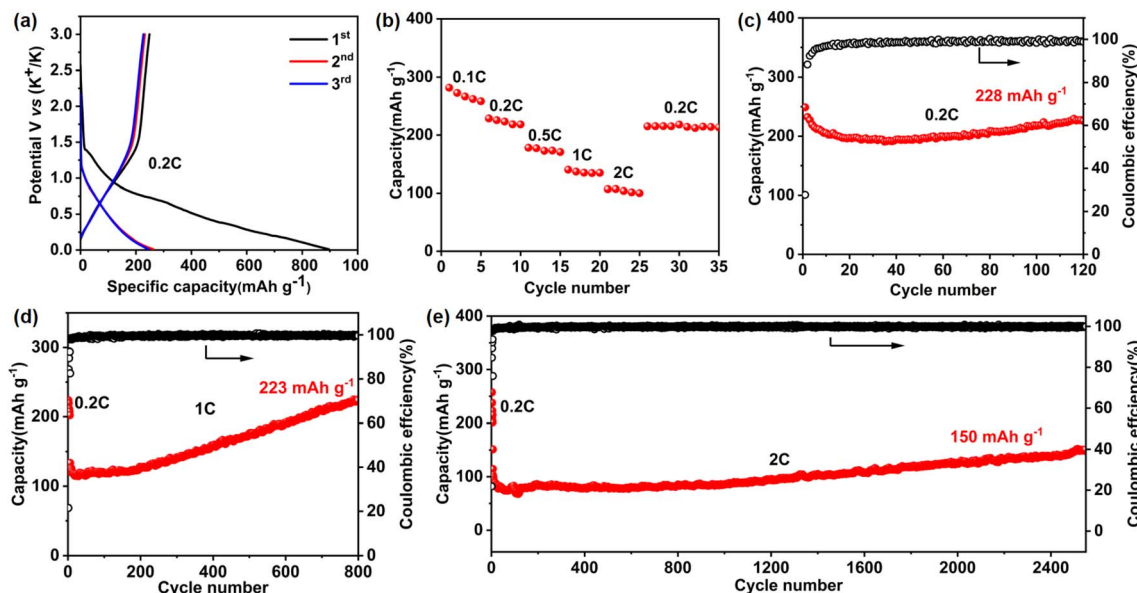

Fig. 2 (a) Charge and discharge profile of Ni–TTF at 0.2C. (b) Charge and discharge of Ni–TTF at various current densities. (c) Cycling performance of Ni–TTF at a current density of 0.2C. (d) Cycling performance of Ni–TTF at a current density of 1C in 800 cycles. (e) Cycling performance of Ni–TTF at a current density of 2C in 2500 cycles.

specific capacity of Ni-TTF recovers to 218 mA h g^{-1}, indicating its impressive rate performance. Cyclic voltammetry (CV) experiments in the first cycles illustrated the irreversible electrochemical reduction peaks occurring at approximately 0.55 V and 1.45 V, which are likely associated with the formation of the solid electrolyte interphase (SEI). We observed reversible reduction peaks near 0.02 V and 0.8 V, accompanied by the corresponding oxidation peaks near 0.3 V and 1 V in the following two cycles, suggesting that the potassium deintercalation process is highly reversible (Fig. S10†).

Most importantly, this Ni-TTF anode could achieve an ultra-stable cyclability when tested at both low current density (such as 0.2C) and high current density (including 1C and 2C, Fig. 2c–e) In the cyclability test at 0.2C, Ni-TTF exhibited an initial reversible capacity of 249 mA h g^{-1}, which slightly decayed to 228 mA h g^{-1} after 120 cycles, corresponding to a capacity retention of 91.6%. In the cycling performance test at 1C for 800 cycles, the specific capacity increased from the initial 133 mA h g^{-1} to 223 mA h g^{-1} (Fig. 2d). An increase in specific capacity was observed, which may be related to several factors, including the gradual activation of deeply buried metal centers and aromatic rings that occurs during the repeated intercalation of alkali metals. Additionally, the widening of the interlayer spacing of covalent organic frameworks (COFs) plays a crucial role in making the electrolyte more permeable and facilitates K$^+$ transport.[23,30] Furthermore, at a high current density of 2C, the specific capacity of the Ni-TTF anode increased from the initial 113 mA h g^{-1} to 150 mA h g^{-1} after 2500 cycles, demonstrating the exceptional stability of the Ni-TTF anode for large-size K-ion storage (Fig. 2e). Meanwhile, the coulombic efficiency can be maintained at a high value of approximately 99.5%, suggesting a highly stable and reversible potassium insertion/extraction process in long-term cycling. To the best of our knowledge, COF anodes for KIBs that can sustain the stable intercalation and deintercalation of large-size K-ions over 2500 cycles without obvious capacity fading are extremely deficient (Table S1†).

To seek a better understanding of the charge storage mechanism, we performed the CV test with device sweep rates, which has been widely considered as an effective technique to identify the ratio of diffusion and capacitive contribution to the capacity. The CV curves are shown in Fig. 3a. The relationship between the peak current (i) and scan rate (v) can be described by using the following equations: $i = av^b$, which could also be

$\log i = b \log v + \log a$, where a and b are arbitrary values. Typically, when $b = 0.5$, it represents a diffusion-controlled process, and as b approaches 1.0, it indicates a closer association with the capacitance-controlled process. For this Ni-TTF anode for KIBs, the calculated values of b for representative cathodic and anodic peaks were 0.87 and 0.73 (Fig. 3b), respectively. These values suggest the existence of a capacitance-controlled process in the rapid transport and storage of K$^+$ ions. The contributions of diffusion and capacitance can be quantified in detail using the following equation: $i(v) = k_1v + k_2v^{1/2}$, where v is the scan rate, and k_1 and k_2 are constants. The term k_1v reflects the capacitance-controlled contribution, while $k_2v^{1/2}$ represents the diffusion-controlled contribution. Furthermore, the equation can also be expressed as $i(v)/v^{1/2} = k_1v^{1/2} + k_2$. This allows us to quantify the proportion values of the capacitance and diffusion contributions by plotting $i(v)/v^{1/2}$ against $v^{1/2}$. With the scan rate increasing from 0.2 to 1 mV s^{-1}, the percentage of capacitance contribution ranged from 44% to 65% (Fig. 3c and S11†). This result indicated that Ni-TTF exhibits obvious capacitance contribution, particularly at different scan rates. The large surface area, continuous porosity, and high electronic conductivity enable Ni-TTF to have a substantial capacitance contribution. Notably, the large capacitance contribution is usually favorable for the fast charge transfer and low strain of the electrode, as a large proportion of K-ions could be stored on the surface and pores of the porous anode, thus explaining well the promising rate capability and outstanding cyclability of this Ni-TTF anode.

To investigate the K$^+$ storage mechanism, we conducted *ex situ* X-ray photoelectron spectroscopy (XPS) analysis of the Ni-TTF anode throughout charge/discharge processes. The high-resolution XPS spectra of the N 1s orbital initially displayed peaks associated with C═N (398.5 eV) and C–N (400 eV) functionalities. After potassiation, the C═N signal transitioned into a C–N signal, suggesting the combination of C═N with K$^+$. Upon recharging to 3 V, the C═N peak increased with the decreasing of the C–N peak, revealing the depotassiation (Fig. S12a†). In the XPS analysis of the S 2p orbital, we observed peaks attributed to S 2p$_{3/2}$ (163.6 eV) and S 2p$_{1/2}$ (164.8 eV) corresponding to C–S, as well as 161.8 eV and 163 eV peaks associated with Ni–S. After discharging to 0.01 V, signals for K–S emerged at 160.4 and 161.5 eV, suggesting the combination of S with K$^+$. After recharging to 3 V, the C–S and Ni–S peaks become
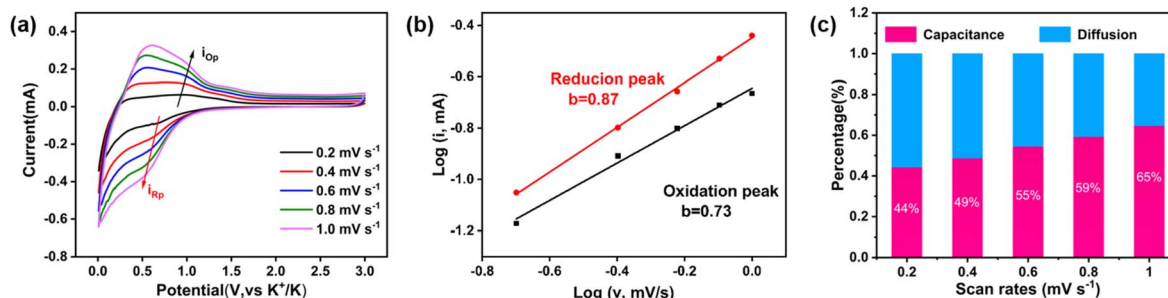

Fig. 3 (a) CV curve of Ni-TTF with scan rates from 0.2–1 mV s^{-1}. (b) b values of cathodic/anodic peaks. (c) Capacitive and diffusion contribution of the K$^+$ ion intercalation and deintercalation process of the Ni-TTF electrode at multiple scan rates of 0.2–1 mV s^{-1}.
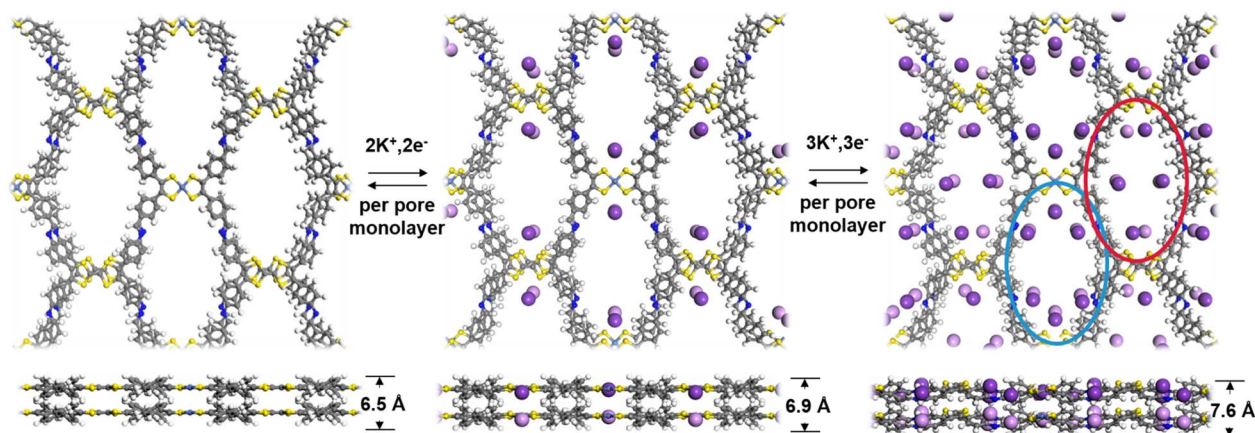
Fig. 4 The proposed two-step K$^+$ ion intercalation and deintercalation process of the Ni–TTF electrode (top view and side view, distances were measured by using the distance of two H atoms from adjacent phenyl rings rotating towards opposite directions). A double-layer view is shown and the K$^+$ ions embedded in the upper and lower layers are shown in dark and light purple color to distinguish. The pores in different chemical environments were highlighted in red and blue circles. Color code: carbon (gray), nitrogen (blue), sulfur (yellow), nickel (iron blue) and potassium (purple).

strong, albeit with reduced intensities compared to their initial state (Fig. S12b†). This observation could be attributed to the partial transformation of the solid electrolyte interface (SEI).[31,32] Significantly, peaks at 165.9 eV, 167.2 eV, 168.2eV and 169.4 eV for the S 2p orbital can be ascribed to the formation of an SEI film containing a S-rich organic/inorganic composite.[31,33,34]

To further understand the K$^+$ storage mechanism, we applied density functional theory (DFT) calculations to evaluate the K$^+$ storage sites and process of the Ni-TTF anode. The electron localization function (ELF), which evaluates the degree of electron localization in different molecular regions of Ni-TTF, was first calculated (Fig. S13†). The ELF values are mapped on the van der Waals surface of Ni-TTF. The blue color regions on this surface map signify significant electron delocalization. As illustrated in Fig. S13,† the delocalization of areas surrounding C=C (in TTF) and Ni atoms inside the pores of the COF is strong, followed by the areas surrounding N atoms and between two propeller-like benzene groups. These observations suggest the existence of multiple favorable K$^+$ storage sites within the Ni-TTF system. We then simulated the K$^+$ ion intercalation and deintercalation process based on a $1 \times 1 \times 2$ supercell model. The intercalation and deintercalation process between K$^+$ and the Ni-TTF framework could be divided into two steps (Fig. 4). In the initial step, K$^+$ ions were clamped by the two adjacent S atoms of NiS$_4$ and TTF units separately, with distances of 3.18 Å for the NiS$_4$ unit and 3.46 Å for the TTF groups (corresponding to 4K$^+$ ions per unit cell). Notably, all the embedded K$^+$ ions aligned closely with the NiS$_4$ unit, resulting in a minor deformation of the Ni-TTF structure in the c-direction, which increased by 0.4 Å for the two layers. In the subsequent step, the N atoms within the Schiff-base groups were able to interact with additional K$^+$ ions, and therefore, the pores containing N atoms (blue circles in Fig. 4) could effectively accommodate 4K$^+$ ions per unit cell. In the other type of pores (red circle in Fig. 4), the region surrounded by two propeller-like benzene groups also exhibited the capacity to interact with K$^+$ ions. However, the

adsorption of 2K$^+$ ions per unit cell in this process induces distortion in the TFF groups, resulting in a staggered arrangement of TTF-bound K$^+$ ions in the two layers. Consequently, the Ni-TTF structure experienced a deformation of 1.2 Å in the c-direction compared to its pure form. Therefore, up to 10K$^+$ could theoretically interact with each repetitive unit, resulting in a theoretical capacity of 233 mA h g^{-1}. Our test showed an experimental specific capacity of 249, 232, and 227 mA h g^{-1} in the first three cycles of this COF anode at asmall current density of 0.2C, respectively. The slight extra capacity in the initial cycle may be related to the formation and decomposition of the electrolyte-derived surface layer and surface capacitance contribution, as revealed by the CV analysis.[35,36] According to the theoretical calculations, Ni-TTF experiences minor deformation in the c-direction, while there is no significant change along the a- and b-directions. This corresponded to a slight extension of the AA stack distance and negligible changes in the shape and diameter of the 1D channel after potassiation. This feature is favorable for structural stability, sufficient exposure of redox-active sites for K$^+$ ion adsorption, and an efficient K$^+$ transfer tunnel, which explains the high-performance electrochemical performance of this COF-based KIB anode.

Conclusions

In summary, a conductive and redox-active COF (Ni-TTF), constructed from Ni-bis(dithiolene) and tetrathiafulvalene (TTF) units, has been successfully synthesized and applied as a promising KIB anode material. The resulting Ni-TTF anode exhibited a high reversible capacity of 223 mA h g^{-1} over more than 800 charge/discharge cycles at a current density of 1C. Moreover, this COF achieved an ultra-stable cyclability without capacity fading after 2500 cycles at 2C. This extraordinary cycling performance surpasses that of state-of-the-art organic KIB anodes. Electrochemical probing and theoretical calculations suggested that the K$^+$ storage mechanism of the Ni-TTF

This journal is © The Royal Society of Chemistry 2023

J. Mater. Chem. A, 2023, **11**, 24661–24666 | **24665**

anode was dominated by a 10-electron redox process based on the crystalline unit cell model, in which the Ni-bis(dithiolene) and tetrathiafulvalene (TTF) units and imine connection sites served as redox-active centers. This research paved a new path for designing porous and redox-active COF materials for ultra-stable KIB anodes.

Author contributions

Y.-Y. Li, D.-S. Bin and J.-L. Zuo conceived and designed the experiments. Y.-Y. Li. and L.-F. Wu performed the synthetic studies. J.-M. Xiao and Y.-F. Chen conducted the electrochemical tests. M. Xie conducted the theoretical calculations. Y.-Y. Li, J.-M. Xiao and Mo Xie discussed and analysed the data. Y.-Y. Li wrote the manuscript. D.-S. Bin, S. Yuan, and J.-L. Zuo revised the manuscript. All authors have given approval to the final version of the manuscript.

Conflicts of interest

There are no conflicts to declare.

Acknowledgements

Notes and references

1 Y. Tian, G. Zeng, A. Rutt, T. Shi, H. Kim, J. Wang, J. Koettgen, Y. Sun, B. Ouyang, T. Chen, Z. Lun, Z. Rong, K. Persson and G. Ceder, *Chem. Rev.*, 2021, **121**, 1623–1669.

2 E. Fan, L. Li, Z. Wang, J. Lin, Y. Huang, Y. Yao, R. Chen and F. Wu, *Chem. Rev.*, 2020, **120**, 7020–7063.

3 B. Dunn, H. Kamath and J. M. Tarascon, *Science*, 2011, **334**, 928–935.

4 K. Song, C. Liu, L. Mi, S. Chou, W. Chen and C. Shen, *Small*, 2021, **17**, e1903194.

5 W. Zhang, Y. Liu and Z. Guo, *Sci. Adv.*, 2019, **5**, eaav7412.

6 K.-Y. Zhang, Z.-Y. Gu, E. H. Ang, J.-Z. Guo, X.-T. Wang, Y. Wang and X.-L. Wu, *Mater. Today*, 2022, **54**, 189–201.

7 W. Zhang, J. Mao, S. Li, Z. Chen and Z. Guo, *J. Am. Chem. Soc.*, 2017, **139**, 3316–3319.

8 S. Dong, Z. Li, Z. Xing, X. Wu, X. Ji and X. Zhang, *ACS Appl. Mater. Interfaces*, 2018, **10**, 15542–15547.

9 M. Lu, K.-F. Wang, H.-D. Ke, Q. Hu, Z.-H. Liu and H.-R. Wu, *Mater. Lett.*, 2018, **232**, 224–227.

10 S. Komaba, T. Hasegawa, M. Dahbi and K. Kubota, *Electrochem. Commun.*, 2015, **60**, 172–175.

11 H. J. Liang, Z. Y. Gu, X. X. Zhao, J. Z. Guo, J. L. Yang, W. H. Li, B. Li, Z. M. Liu, Z. H. Sun, J. P. Zhang and X. L. Wu, *Sci. Bull.*, 2022, **67**, 1581–1588.

12 D. S. Bin, X. J. Lin, Y. G. Sun, Y. S. Xu, K. Zhang, A. M. Cao and L. J. Wan, *J. Am. Chem. Soc.*, 2018, **140**, 7127–7134.

13 J. Lin, S. Lu, Y. Zhang, L. Zeng, Y. Zhang and H. Fan, *J. Colloid Interface Sci.*, 2023, **645**, 654–662.

14 M. Wang, B. Qin, F. Xu, W. Yang, Z. Liu, Y. Zhang and H. Fan, *J. Colloid Interface Sci.*, 2023, **650**, 446–455.

15 Q. Wang, X. Zhao, C. Ni, H. Tian, J. Li, Z. Zhang, S. X. Mao, J. Wang and Y. Xu, *J. Phys. Chem. C*, 2017, **121**, 12652–12657.

16 Q. Pan, Y. Zheng, Z. Tong, L. Shi and Y. Tang, *Angew. Chem., Int. Ed.*, 2021, **60**, 11835–11840.

17 C. Peng, G.-H. Ning, J. Su, G. Zhong, W. Tang, B. Tian, C. Su, D. Yu, L. Zu, J. Yang, M.-F. Ng, Y.-S. Hu, Y. Yang, M. Armand and K. P. Loh, *Nat. Energy*, 2017, **2**, 17074.

18 Q. Deng, S.-J. He, J. Pei, C. Fan, C. Li, B. Cao, Z.-H. Lu and J. Li, *Electrochem. Commun.*, 2017, **75**, 29–32.

19 C. Luo, O. Borodin, X. Ji, S. Hou, K. J. Gaskell, X. Fan, J. Chen, T. Deng, R. Wang, J. Jiang and C. Wang, *Proc. Natl. Acad. Sci. U. S. A.*, 2018, **115**, 2004–2009.

20 M. S. Lohse and T. Bein, *Adv. Funct. Mater.*, 2018, **28**, 1705553.

21 Q. Zhang, H. Wei, L. Wang, J. Wang, L. Fan, H. Ding, J. Lei, X. Yu and B. Lu, *ACS Appl. Mater. Interfaces*, 2019, **11**, 44352–44359.

22 R. Shi, L. Liu, Y. Lu, C. Wang, Y. Li, L. Li, Z. Yan and J. Chen, *Nat. Commun.*, 2020, **11**, 178.

23 Z. Lei, Q. Yang, Y. Xu, S. Guo, W. Sun, H. Liu, L. P. Lv, Y. Zhang and Y. Wang, *Nat. Commun.*, 2018, **9**, 576.

24 Z. Luo, L. Liu, J. Ning, K. Lei, Y. Lu, F. Li and J. Chen, *Angew Chem. Int. Ed. Engl.*, 2018, **57**, 9443–9446.

25 J. Su, W. He, X.-M. Li, L. Sun, H.-Y. Wang, Y.-Q. Lan, M. Ding and J.-L. Zuo, *Matter*, 2020, **2**, 711–722.

26 S. S. Park, E. R. Hontz, L. Sun, C. H. Hendon, A. Walsh, T. Van Voorhis and M. Dinca, *J. Am. Chem. Soc.*, 2015, **137**, 1774–1777.

27 M. Lu, J. Liu, Q. Li, M. Zhang, M. Liu, J. L. Wang, D. Q. Yuan and Y. Q. Lan, *Angew. Chem., Int. Ed.*, 2019, **58**, 12392–12397.

28 S.-L. Cai, Y.-B. Zhang, A. B. Pun, B. He, J. Yang, F. M. Toma, I. D. Sharp, O. M. Yaghi, J. Fan, S.-R. Zheng, W.-G. Zhang and Y. Liu, *Chem. Sci.*, 2014, **5**, 4693–4700.

29 Y. Y. Li, T. Wei, C. Liu, Z. Zhang, L. F. Wu, M. Ding, S. Yuan, J. Zhu and J. L. Zuo, *Chem. – Eur. J.*, 2023, **29**, e202301048.

30 W. Sun, X. Tang, Q. Yang, Y. Xu, F. Wu, S. Guo, Y. Zhang, M. Wu and Y. Wang, *Adv. Mater.*, 2019, **31**, e1903176.

31 G.-Z. Yang, Y.-F. Chen, B.-Q. Feng, C.-X. Ye, X.-B. Ye, H. Jin, E. Zhou, X. Zeng, Z.-L. Zheng, X.-L. Chen, D.-S. Bin and A.-M. Cao, *Energy Environ. Sci.*, 2023, **16**, 1540–1547.

32 R. Ma, L. Fan, J. Wang and B. Lu, *Electrochim. Acta*, 2019, **293**, 191–198.

33 L. Fan, S. Chen, R. Ma, J. Wang, L. Wang, Q. Zhang, E. Zhang, Z. Liu and B. Lu, *Small*, 2018, **14**, e1801806.

34 S. Liu, J. Mao, Q. Zhang, Z. Wang, W. K. Pang, L. Zhang, A. Du, V. Sencadas, W. Zhang and Z. Guo, *Angew. Chem., Int. Ed.*, 2020, **59**, 3638–3644.

35 H. Kim, W. Choi, J. Yoon, J. H. Um, W. Lee, J. Kim, J. Cabana and W. S. Yoon, *Chem. Rev.*, 2020, **120**, 6934–6976.

36 J. Yan, Y. Cui, M. Xie, G. Z. Yang, D. S. Bin and D. Li, *Angew. Chem., Int. Ed.*, 2021, **60**, 24467–24472.

24666 | *J. Mater. Chem. A*, 2023, **11**, 24661–24666

This journal is © The Royal Society of Chemistry 2023